Author Manuscript
Accepted for publication in a peer-reviewed journal

NIST National Institute of Standards and Technology • U.S. Department of Commerce

Published in final edited form as:
Appl Phys Lett. 2019 ; 115(12): .

High spin-wave propagation length consistent with low damping in a metallic ferromagnet

Luis Flacke[1,2,a)], **Lukas Liensberger**[1,2], **Matthias Althammer**[1,2], **Hans Huebl**[1,2,3,4], **Stephan Geprägs**[1], **Katrin Schultheiss**[5], **Aleksandr Buzdakov**[5], **Tobias Hula**[5], **Helmut Schultheiss**[5], **Eric R. J. Edwards**[6], **Hans T. Nembach**[6], **Justin M. Shaw**[6], **Rudolf Gross**[1,2,3,4], **Mathias Weiler**[1,2,b)]

[1]Walther-Meißner Institute, Bayerische Akademie der Wissenschaften, 85748 Garching, Germany

[2]Physics Department, Technical University of Munich, 85748 Garching, Germany

[3]Nanosystems Initiative Munich, 80799 Munich, Germany

[4]Munich Center for Quantum Science and Technology (MCQST), 80799 Munich, Germany

[5]Helmholtz-Zentrum Dresden-Rossendorf, 01328 Dresden, Germany

[6]Quantum Electromagnetics Division, National Institute of Standards and Technology, Boulder, Colorado 80305, USA

Abstract

We report ultralow intrinsic magnetic damping in $Co_{25}Fe_{75}$ heterostructures, reaching the low 10^{-4} regime at room temperature. By using a broadband ferromagnetic resonance technique in out-of-plane geometry, we extracted the dynamic magnetic properties of several $Co_{25}Fe_{75}$-based heterostructures with varying ferromagnetic layer thicknesses. By measuring radiative damping and spin pumping effects, we found the intrinsic damping of a 26 nm thick sample to be $\alpha_0 \lesssim 3.18 \times 10^{-4}$. Furthermore, using Brillouin light scattering microscopy, we measured spin-wave propagation lengths of up to $(21 \pm 1)\ \mu$m in a 26 nm thick $Co_{25}Fe_{75}$ heterostructure at room temperature, which is in excellent agreement with the measured damping.

Itinerant ferromagnets (FMs) are advantageous for spintronic and magnonic devices. They benefit from, e.g., large magnetoresistive effects and current-induced spin–orbit torques.[1] In many magnetoresistive technologies (e.g., anisotropic magnetoresistance, giant magnetoresistance, and tunnel magnetoresistance), electronic conductivity is indispensable. Moreover, due to high saturation magnetization in metallic FMs, spin-wave (SW) group velocities are in general significantly higher than those in insulating ferrimagnets.[2–5] High saturation magnetizations in general are easily detectable. Nevertheless, itinerant FMs typically have considerable magnetic damping.[6,7] This is unfavorable for many applications. For example, low damping is crucial for oscillators based on spin transfer torques and spin–orbit torques as well as for achieving large spin-wave propagation lengths (SWPLs).[8–10] The need for thin film materials with low magnetic damping has triggered the interest in the

a) luis.flacke@wmi.badw.de. b) mathias.weiler@wmi.badw.de.

insulating ferrimagnet yttrium-iron garnet ($Y_3Fe_5O_{12}$, YIG).[11–13] Although for YIG, very small total (Gilbert) damping parameters on the order of $\alpha_G \approx 10^{-5}$ and large SWPLs of a few tens of micrometers (up to ~25μm) in thin films (~20 nm) have been reported,[5,13,14] its insulating properties and requirement for crystalline growth are challenges for large scale magnonic applications.

Schoen *et al.* recently observed ultralow intrinsic magnetic damping in $Co_{25}Fe_{75}$ (CoFe) metallic thin films [$\alpha_0 = (5\pm1{:}8) \times 10^{-4}$],[15] and Körner *et al.* reported PLs of 5 μm – 8 μm in CoFe using time resolved scanning magneto-optical Kerr microscopy.[4] This motivated our study on sputter-deposited CoFe-based thin film heterostructures. We use broadband ferromagnetic resonance (BB-FMR) spectroscopy[16] in out-of-plane (OOP) geometry and Brillouin light scattering (BLS) microscopy[17] and find intrinsic damping parameters in the lower 10^{-4} regime as well as SWPLs of more than 20 μm. The damping is therefore comparable to YIG/heavy metal (HM) heterostructures,[18] and the SWPL is comparable to that of state-of-the-art YIG thin films.[5,13] Thin film CoFe is a promising candidate for all-metal magnonic devices, as it combines low magnetic damping with good electrical conductivity and large saturation magnetization, while enabling easy fabrication by room-temperature processing/deposition, no required annealing, polycrystalline structure, and scalability to the nanometer regime.

For BB-FMR, Ta(3 nm)/Al(3 nm)/$Co_{25}Fe_{75}(t)$/Al(3 nm)/Ta(3 nm) heterostructures with different thicknesses t of the CoFe layer were sputter deposited on a thermally oxidized Si (100) substrate at an Ar pressure of 5×10^{-6} bar at room temperature. No subsequent annealing process was performed. The CoFe layer thickness was varied in the range of 1.4 nm < t < 26 nm as determined by X-ray reflectometry.

The OOP BB-FMR measurements were performed at room temperature using a vector network analyzer (VNA). This geometry was chosen to determine the intrinsic magnetic damping without further damping contributions due to magnon-magnon scattering.[19] The samples were placed directly on a coplanar waveguide (CPW), with an 80 μm wide center conductor. For the measurements, the VNA frequency f was kept constant and the microwave transmission parameter S_{21} was recorded as a function of applied magnetic field H_0 for a range of frequencies at a VNA output power of 0 dBm. A representative set of data as measured for the real and imaginary part of S_{21} at 16GHz for samples with t = 1.8 nm and t = 26 nm is shown in Figs. 1(a) and 1(b).

The magnetic response of the thin film FM magnetized out-of-plane is given by the susceptibility χ which is obtained by solving the Landau-Lifshitz-Gilbert (LLG) equation,[15,20]

$$\chi(H_0) = \frac{M_s(H_0 - H_{\mathrm{res}} + H_{\mathrm{eff}})}{\left(H_0 - H_{\mathrm{res}} + H_{\mathrm{eff}} + i\frac{\Delta H}{2}\right)^2 - H_{\mathrm{eff}}^2} \quad (1)$$

.

Here, M_s is the saturation magnetization, H_{res} is the resonance field, $H_{eff} = 2\pi f / (\mu_0 \gamma)$, with γ being the gyromagnetic ratio, and $\Delta H = 2(2\pi f \alpha)/(\gamma \mu_0)$ is the full width at half maximum (FWHM) line-width of the resonance. The data in Figs. 1(a) and 1(b) are fitted to[21]

$$S_{21}(H_0) = S_{21}^0 + iA\frac{\chi(H_0)}{M_s} = S_{21}^0(1 + \Delta S_{21}) \quad (2)$$

,

where S_{21}^0 is the background transmission through the CPW without the magnetic resonance peak. It is determined from the fits as a complex linear background to the data $S_{21}^0(H_0) = S_{21}^a + H_0 S_{21}^b$. Factor A is a complex-valued scaling parameter.

In the OOP geometry, the resonance condition for thin films is given by[22]

$$\mu_0 H_{res} = \mu_0 M_{eff} + \mu_0 H_{eff} \quad (3)$$

,

where $M_{eff} = M_s - H_k$ is the effective magnetization, with the uniaxial out-of-plane anisotropy field H_k. In Fig. 1(c), we plot the determined H_{res} vs the frequency f. From the fit to Eq. (3) [red solid lines in Fig. 1(c)], we obtain M_{eff} and γ of the specific sample.

The FWHM linewidth vs frequency data shown in Fig. 1(d) are fitted to

$$\mu_0 \Delta H = \mu_0 H_{inh} + 2 \cdot \frac{2\pi f \alpha_G}{\gamma} \quad (4)$$

.

Here, H_{inh} is the inhomogeneous linewidth broadening and α_G is the phenomenological Gilbert damping parameter.[23,24] H_{inh} indicates the presence of long-range magnetic inhomogeneities, which become more relevant for thinner films but do not contribute to our α_G.

Several contributions to the measured total damping (α_G) were extracted from our data. In addition to the intrinsic damping of the magnetic material itself (α_0), spin pumping (α_{sp}) contributes significantly[25–27] to the total damping in our thinner heterostructures due to the adjacent HM (Ta) layers. Furthermore, we consider additional damping contributions from eddy currents (α_{eddy}) and radiative damping (α_{rad}).[15,21] Due to these contributions, the total damping ($\alpha_G = \alpha_0 + \alpha_{sp} + \alpha_{eddy} + \alpha_{rad}$) depends on the FM thickness. We calculated damping due to eddy currents and measured radiative damping contributions to the total damping. The eddy current contribution is given by[15] $\alpha_{eddy} = \gamma \mu_0^2 M_s t^2 / 16\rho$. Here, $\mu_0 M_s$ = 2.35 T (see the supplementary material) and ρ = 340 nΩ m is the estimated weighted resistivity value of the CoFe film derived from the resistivities of iron and cobalt thin films with thicknesses of around 20 nm.[28,29] With these values, we find an almost negligible eddy current contribution to the total damping. A quantitative determination analogous to Ref. 21 of the radiative damping is done by analyzing the magnitude of the measured inductance L of all samples. The quantification of this contribution is important for BB-FMR because it

represents a damping by inductive power dissipation into the CPW and, hence, is not a property of the sample itself but depends on the setup. In possible applications like, e.g., magnonic waveguides or spin-Hall nano-oscillators, this contribution vanishes and the damping lowers by α_{rad}. With Eq. (2) in this work and Eq. (9) from Ref. 21, one obtains

$$\frac{L}{\chi} \equiv \tilde{L} = -\frac{2Z_0 A}{M_s S_{21}^0 \omega} \tag{5}$$

.

Here, $Z_0 = 50\ \Omega$ is the CPW impedance. It has been shown that $\tilde{L} = \tilde{L}_0 + \tilde{L}_1(\omega)$, where $\tilde{L}_0 \in \mathbb{R}$ and $\tilde{L}_1 \in \mathbb{C}$, due to the effect of inverse spin–orbit torques.[21] We extract L from the FMR measurements, and the dipolar inductance $\tilde{L}_0$ from a fit of $\tilde{L}$ vs f for each sample. The radiative damping contribution is then given as[15]

$$\alpha_{\mathrm{rad}} = \frac{1}{4}\frac{\gamma \mu_0 M_s}{Z_0}\tilde{L}_0 \tag{6}$$

.

This analysis allows us to determine α_{rad} independent of geometrical parameters of the samples or CPWs and is used to quantitatively extract the dipolar inductance without any calibration of the microwave circuit. For the thickest sample, we obtain $\alpha_{\mathrm{rad}} = (4.69 \pm 0{:}05) \times 10^{-4}$, which is comparable to the previously obtained values.[15,30] The damping including the spin pumping contribution α_{sp} is given by

$$\alpha_0 + \alpha_{\mathrm{sp}} = \alpha_0 + 2\frac{\gamma \hbar g_{\mathrm{eff}}^{\uparrow\downarrow}}{4\pi M_s}\frac{1}{t} \tag{7}$$

.

where $g_{\mathrm{eff}}^{\uparrow\downarrow}$ is the effective spin mixing conductance.[30] We subtract α_{rad} and α_{eddy} from the measured total damping α_G [see Figs. 2(a) and 2(b)] and plot the remaining damping $\alpha_0 + \alpha_{\mathrm{sp}}$ as a function of $1/t$ in Fig. 2(b) together with the total damping α_G. From a linear fit [Eq. (7)] to $\alpha_0 + \alpha_{\mathrm{sp}}$, we obtain g_{eff} and α_0. Therefore, we use M_s as above and $\gamma/2\pi = 28.65$ GHz/T. The fitted $g_{\mathrm{eff}} = (5.5 \pm 0.3) \times 10^{18}\ \mathrm{m}^{-2}$ is in agreement with literature values.[15] The y-intercept indicating the extrapolated intrinsic damping yields $\alpha_0 = (0.91 \pm 1.69)\ 10^{-4}$, and hence, the intrinsic damping is below the sensitivity of our approach. For the thickest sample $t = 26$ nm shown in Fig. 2(a), we obtain $\alpha_0 = (3.18 \pm 0.48)\ 10^{-4}$ (see the supplementary material for details). Within the errors, this value lies close to the extrapolated value and is the lowest intrinsic damping for a thin film ferromagnetic metal reported so far. We attribute the slightly reduced intrinsic α_0 compared to Ref. 30 to the use of a different seed layer, which has a substantial impact on the damping of CoFe.[31]

The low damping properties of the CoFe heterostructures, in combination with the high saturation magnetization, are expected to result in long PLs of dipolar SWs. We use

microfocused BLS[17] to study the SW propagation in patterned CoFe samples, which is schematically depicted in Figs. 3(a) and 3(b).

For our experiments, we fabricated patterned stripes of a Pt(3 nm)/Cu(3 nm)/$Co_{25}Fe_{75}(t)$/Cu(3 nm)/Ta(3 nm) heterostructure using laser (sample A) and electron beam (sample B) lithography, sputter deposition, and a subsequent lift-off process. This stack sequence was used as lower in-plane damping was observed compared to the samples containing Al. Below, we present data on only two samples with a thickness of $t = 5$ nm and a width of $w = 1.5\ \mu$m for sample A and $t = 26$ nm and $w = 5\ \mu$m for sample B, respectively. An aluminum antenna was placed on top of the CoFe strip to drive spin dynamics via a microwave drive applied to the antenna. For sample A, we used a simple aluminum strip optimized for excitation of the uniform (FMR) mode, whereas for sample B, we used a CPW antenna optimized for an efficient excitation of SWs with wave number $k \leq 2\ \mu m^{-1}$.

In order to compare the uniform FMR-mode linewidths of the extended and patterned films, we used sample A in backward volume geometry and placed the laser spot close to the antenna, where the FMR mode is dominantly excited. We recorded BLS spectra for several magnetic fields for each frequency. The BLS intensity is integrated, and the signal sum is then plotted vs the external magnetic field in Fig. 3(c). The FWHM-linewidth ΔH is determined by fitting a Lorentzian (red line). We then compared the fitted linewidth with the measured in-plane BB-FMR linewidth of a blanket film, deposited simultaneously with the structured BLS sample. In the in-plane configuration, the total damping increases due to magnon-magnon scattering[19,33] and possible anisotropic damping.[34–37] As shown in Fig. 3(d), the linewidths $\mu_0\Delta H$ determined from BB-FMR (black symbols) and BLS (blue symbols) are very similar, indicating that the damping properties are not affected by the patterning, as expected in a lift-off process with micrometer feature sizes.

In the next set of experiments, we investigate the SWPL of sample B [see Fig. 3(b)]. Here, the magnitude of the external magnetic field was fixed at $\mu_0 H_0 = 43$ mT, while the field was applied perpendicular to the CoFe strip (Damon-Eshbach geometry). The BLS intensity was recorded as a function of position (x, y) over the CoFe strip. The BLS intensity decay in the x direction (i.e., the BLS intensity averaged over the width of the strip in order to suppress mode-beating effects[38–40]) is shown in Fig. 3(e) for $f = 9.5$GHz. The SWPL λ_{prop} is extracted by a fit to $I = I_0 \exp(-2x/\lambda_{prop})$[41] and plotted vs f in Fig. 3(f). From our experiments, we extract a maximum SWPL of $(21 \pm 1)\ \mu$m, well exceeding the previously obtained results for FeNi alloys[42] and CoFe[4] and very comparable to values found for YIG thin films.[5,13] The red curve is the theoretical prediction, based on the analytical Kalinikos-Slavin model detailed below and using the magnetic parameters determined by in-plane BB-FMR ($\mu_0 M_s = 2.35$ T, $\mu_0 M_{eff} = 2.29$ T, $\alpha_G - \alpha_{rad} = 3.92 \times 10^{-3}$, and $g = 2.051$) for a codeposited reference sample (see the supplementary material).

Starting with a simplified version of Kalinikos and Slavin's SW dispersion for the modes with $\mathbf{k}_x \perp \mathbf{M}$,[43,44]

$$f_{res} = \frac{\mu_o \gamma}{2\pi}\sqrt{H_0 + H_d + H_k + M_s\frac{1-\exp(-kt)}{kt}} \times \sqrt{H_0 + H_d + M_s\left(1 - \frac{1-\exp-(-kt)}{kt}\right)}, \quad (8)$$

we calculated the group velocity $\upsilon_g = 2\pi\partial f_{res}/\partial k$. Here, $k = \sqrt{k_x^2 + k_y^2}$ is the in-plane wave vector of the traveling SW and $\mu_0 H_k = \mu_0 M_{eff} - \mu_0 M_s = -60$ mT is the effective interface anisotropy field. The calculation of the transversal wave vector component $k_y = 0.31\ \mu m^{-1}$ due to geometrical confinement was shown to be nontrivial and is used as a fitting parameter, as in Ref. 45. The resonance linewidth is given by[46] $\Delta\omega = \alpha\mu_0\gamma(M_{eff}/2 + H_0 + H_d)$, and the lifetime of the SW is $\tau = 1/\Delta\omega$. Here, $\alpha = \alpha_G - \alpha_{rad}$. The SWPL is $\lambda_{prop} = \upsilon_g\tau$. The demagnetization field in the *y*-direction was set to $\mu_0 H_d = -18$ mT, as required for matching Eq. (8) to the SW dispersion obtained by phase-resolved μBLS[17] [see Fig. 3(g)]. This value for H_d is in good agreement with the demagnetization ($\mu_0 H_d \approx -12$ mT) obtained for an ellipsoid with the axes corresponding to the CoFe-stripe dimensions.[47] We find excellent agreement between this model and our experimental data in Fig. 3(f).

In summary, our sputter-deposited $Co_{25}Fe_{75}$ layers exhibit a record low intrinsic damping for metallic thin film ferromagnets of $\alpha_0 \lesssim 3.18 \times 10^{-4}$ in OOP geometry. The damping properties of extended films are maintained for micropatterned films, and spin-wave propagation lengths are in very good agreement with the properties extracted from BB-FMR. The low magnetic damping, together with the high saturation magnetization, leads to spin-wave decay lengths of more than 20 μm at room temperature, which is the highest reported so far in itinerant magnetic systems. This property makes $Co_{25}Fe_{75}$ a promising material for all-metal spintronic and magnonic devices, compatible with semiconductor technology.

See the supplementary material for (I) the determination of the saturation magnetization M_s, (II) a detailed linewidth analysis of the $t = 26$ nm sample, and (III) IP BB-FMR data of the reference sample for optical measurements.

Supplementary Material

Refer to Web version on PubMed Central for supplementary material.

Acknowledgments

We acknowledge financial support of the Deutsche Forschungsgemeinschaft (DFG, German Research Foundation) via Nos. WE5386/4, WE5386/5, and SCHU2922/1 and Germany's Excellence Strategy No. EXC-2111-390814868.

REFERENCES

1. Gambardella P and Miron IM, Philos. Trans. R. Soc., A 369, 3175 (2011).
2. Wessels P, Vogel A, Tödt JN, Wieland M, Meier G, and Drescher M, Sci. Rep 6, 22117 (2016). [PubMed: 26906113]
3. Talalaevskij A, Decker M, Stigloher J, Mitra A, Körner HS, Cespedes O, Back CH, and Hickey BJ, Phys. Rev. B 95, 064409 (2017).

4. Körner HS, Schoen MAW, Mayer T, Decker MM, Stigloher J, Weindler T, Meier TNG, Kronseder M, and Back CH, Appl. Phys. Lett 111, 132406 (2017).
5. Collet M, Gladii O, Evelt M, Bessonov V, Soumah L, Bortolotti P, Demokritov SO, Henry Y, Cros V, Bailleul M, Demidov VE, and Anane A, Appl. Phys. Lett 110, 092408 (2017).
6. Maksymov IS and Kostylev M, Physica E 69, 253 (2015).
7. Twisselmann DJ and McMichael RD, J. Appl. Phys. 93, 6903 (2003).
8. Demidov VE, Urazhdin S, Zholud A, Sadovnikov AV, and Demokritov SO, Appl. Phys. Lett. 105, 172410 (2014).
9. Kruglyak VV, Demokritov SO, and Grundler D, J. Phys. D 43, 264001 (2010).
10. Chumak AV, Vasyuchka VI, Serga AA, and Hillebrands B, Nat. Phys 11, 453 (2015).
11. Hauser C, Richter T, Homonnay N, Eisenschmidt C, Qaid M, Deniz H, Hesse D, Sawicki M, Ebbinghaus SG, and Schmidt G, Sci. Rep 6, 20827 (2016). [PubMed: 26860816]
12. Evelt M, Demidov VE, Bessonov V, Demokritov SO, Prieto JL, Muñoz M, Ben Youssef J, Naletov VV, de Loubens G, Klein O, Collet M, Garcia-Hernandez K, Bortolotti P, Cros V, and Anane A, Appl. Phys. Lett 108, 172406 (2016).
13. Jungfleisch MB, Zhang W, Jiang W, Chang H, Sklenar J, Wu SM, Pearson JE, Bhattacharya A, Ketterson JB, Wu M, and Hoffmann A, J. Appl. Phys 117, 17D128 (2015).
14. Chang H, Li P, Zhang W, Liu T, Hoffmann A, Deng L, and Wu M, IEEE Magn. Lett 5, 6700104 (2014).
15. Schoen MAW, Shaw JM, Nembach HT, Weiler M, and Silva TJ, Phys. Rev. B 92, 184417 (2015).
16. Kalarickal SS, Krivosik P, Wu M, Patton CE, Schneider ML, Kabos P, Silva TJ, and Nibarger JP, J. Appl. Phys 99, 093909 (2006).
17. Sebastian T, Schultheiss K, Obry B, Hillebrands B, and Schultheiss H, Front. Phys 3, 35 (2015).
18. Sun Y, Chang H, Kabatek M, Song YY, Wang Z, Jantz M, Schneider W, Wu M, Montoya E, Kardasz B, Heinrich B, Te Velthuis SG, Schultheiss H, and Hoffmann A, Phys. Rev. Lett 111, 106601 (2013).
19. Hillebrands B and Ounadjela K, Spin Dynamics in Confined Magnetic Structures II, Topics in Applied Physics Vol. 87, edited by Hillebrands B and Ounadjela K (Springer Berlin Heidelberg, Berlin, Heidelberg, 2003).
20. Nembach HT, Silva TJ, Shaw JM, Schneider ML, Carey MJ, Maat S, and Childress JR, Phys. Rev. B 84, 054424 (2011).
21. Berger AJ, Edwards ERJ, Nembach HT, Karenowska AD, Weiler M, and Silva TJ, Phys. Rev. B 97, 094407 (2018).
22. Kittel C, Phys. Rev 73, 155 (1948).
23. Woltersdorf G, Hoffmann F, Bauer HG, and Back CH, Phys. Rev. B 87, 054422 (2013).
24. McMichael RD, Twisselmann DJ, and Kunz A, Phys. Rev. Lett 90, 227601 (2003).
25. Tserkovnyak Y, Brataas A, and Bauer GEW, Phys. Rev. Lett 88, 117601 (2002).
26. Haertinger M, Back CH, Lotze J, Weiler M, Geprägs S, Huebl H, Goennenwein STB, and Woltersdorf G, Phys. Rev. B 92, 054437 (2015).
27. Brataas A, Tserkovnyak Y, Bauer GEW, and Kelly PJ, Spin Current (Oxford University Press, 2017), Vol. 1, pp. 93–142.
28. Raeburn SJ and Aldridge RV, J. Phys. F 8, 1917 (1978).
29. De Vries JW, Thin Solid Films 167, 25 (1988).
30. Schoen MAW, Thonig D, Schneider ML, Silva TJ, Nembach HT, Eriksson O, Karis O, and Shaw JM, Nat. Phys 12, 839 (2016).
31. Edwards ER, Nembach HT, and Shaw JM, Phys. Rev. Appl 11, 054036 (2019).
32. Shaw JM, Nembach HT, Silva TJ, and Boone CT, J. Appl. Phys 114, 243906 (2013).
33. Arias R and Mills DL, Phys. Rev. B 60, 7395 (1999).
34. Chen L, Mankovsky S, Wimmer S, Schoen MAW, Körner HS, Kronseder M, Schuh D, Bougeard D, Ebert H, Weiss D, and Back CH, Nat. Phys 14, 490 (2018).
35. Seib J, Steiauf D, and Fähnle M, Phys. Rev. B 79, 092418 (2009).
36. Steiauf D and Fähnle M, Phys. Rev. B 72, 064450 (2005).

37. Safonov VL, J. Appl. Phys 91, 8653 (2002).
38. Pirro P, Brächer T, Vogt K, Obry B, Schultheiss H, Leven B, and Hillebrands B, Phys. Status Solidi B 248, 2404 (2011).
39. Demidov VE, Kostylev MP, Rott K, Krzysteczko P, Reiss G, and Demokritov SO, Appl. Phys. Lett 95, 112509 (2009).
40. Clausen P, Vogt K, Schultheiss H, Schäfer S, Obry B, Wolf G, Pirro P, Leven B, and Hillebrands B, Appl. Phys. Lett 99, 162505 (2011).
41. Demidov VE, Urazhdin S, Liu R, Divinskiy B, Telegin A, and Demokritov SO, Nat. Commun 7, 10446 (2016). [PubMed: 26818232]
42. Yamanoi K, Yakata S, Kimura T, and Manago T, Jpn. J. Appl. Phys., Part 1 52, 083001 (2013).
43. Kalinikos BA and Slavin AN, J. Phys. C 19, 7013 (1986).
44. Liensberger L, Flacke L, Rogerson D, Althammer M, Gross R, and Weiler M, IEEE Magn. Lett 10, 5503905 (2019).
45. Duan Z, Krivorotov IN, Arias RE, Reckers N, Stienen S, and Lindner J, Phys. Rev. B 92, 104424 (2015).
46. Stancil DD and Prabhakar A, Spin Waves (Springer, Boston, MA, 2009), p. 332.
47. Osborn JA, Phys. Rev 67, 351 (1945).

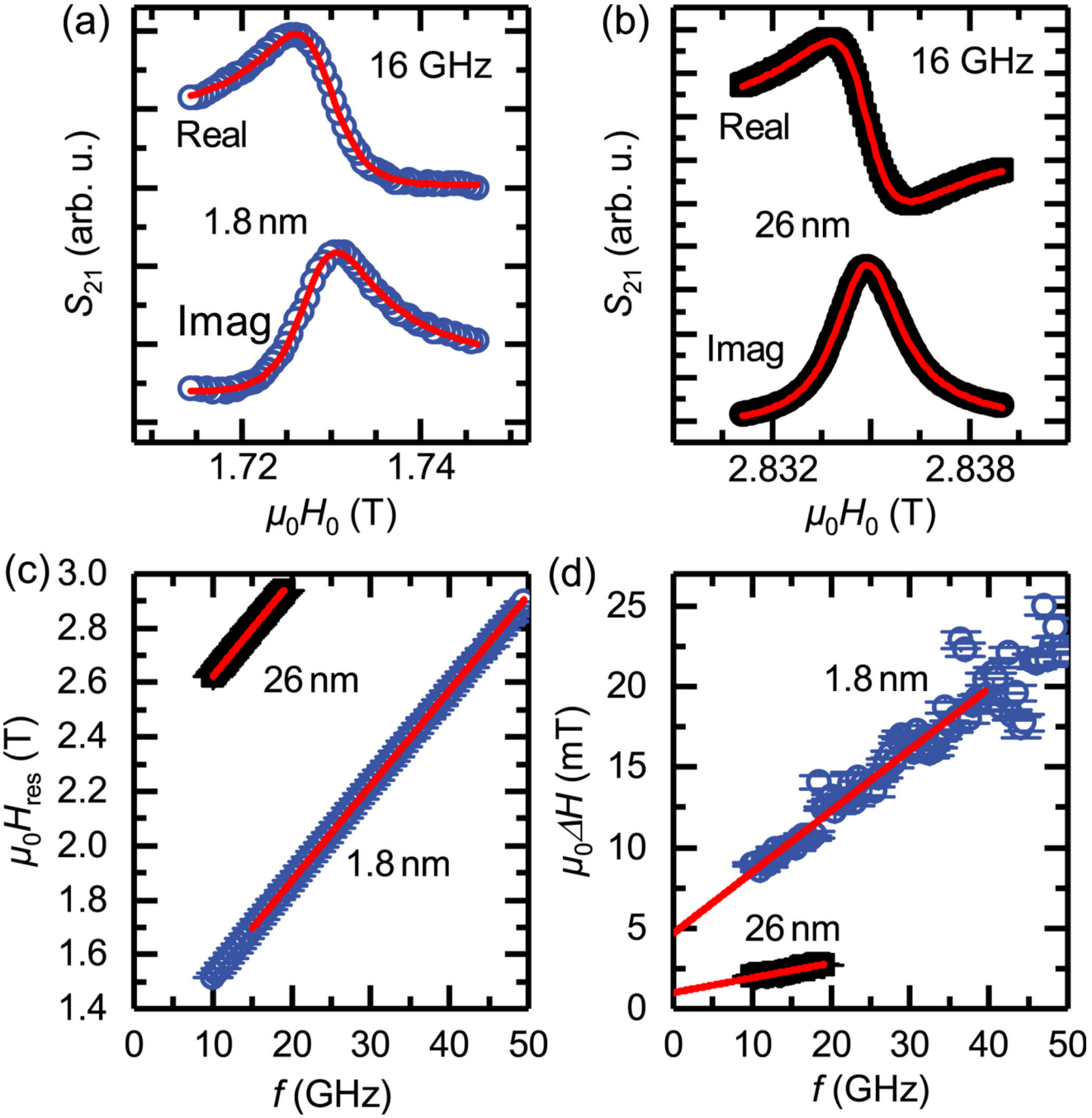

FIG. 1.

(a) Measured microwave transmission S_{21} at 16 GHz vs applied OOP magnetic field H_0 for blanket Ta(3 nm)/Al(3 nm)/$Co_{25}Fe_{75}(t)$/Al(3 nm)/Ta(3 nm) samples with CoFe thickness t = 1.8 nm [(a) blue symbols] and t = 26 nm [(b) black symbols], respectively. The red lines are fits of Eq. (2) to the data. The extracted resonance fields H_{res} and linewidths ΔH as a function of the applied microwave frequency are shown in (c) and (d), respectively. Here, the error bars (smaller than the symbol size) are extracted fit errors from (a) and (b). In (c), the red line is a fit to Eq. (3) to extract the Landé-factor g and the effective magnetization M_{eff}.

In (d), the linewidth is plotted vs frequency. The Gilbert parameter α_G and the inhomogeneous linewidth broadening H_{inh} are extracted by fitting the data to Eq. (4) (red lines). The linewidth of the $t = 26$ nm thick sample is shown in Fig. 2(c) on an expanded scale.

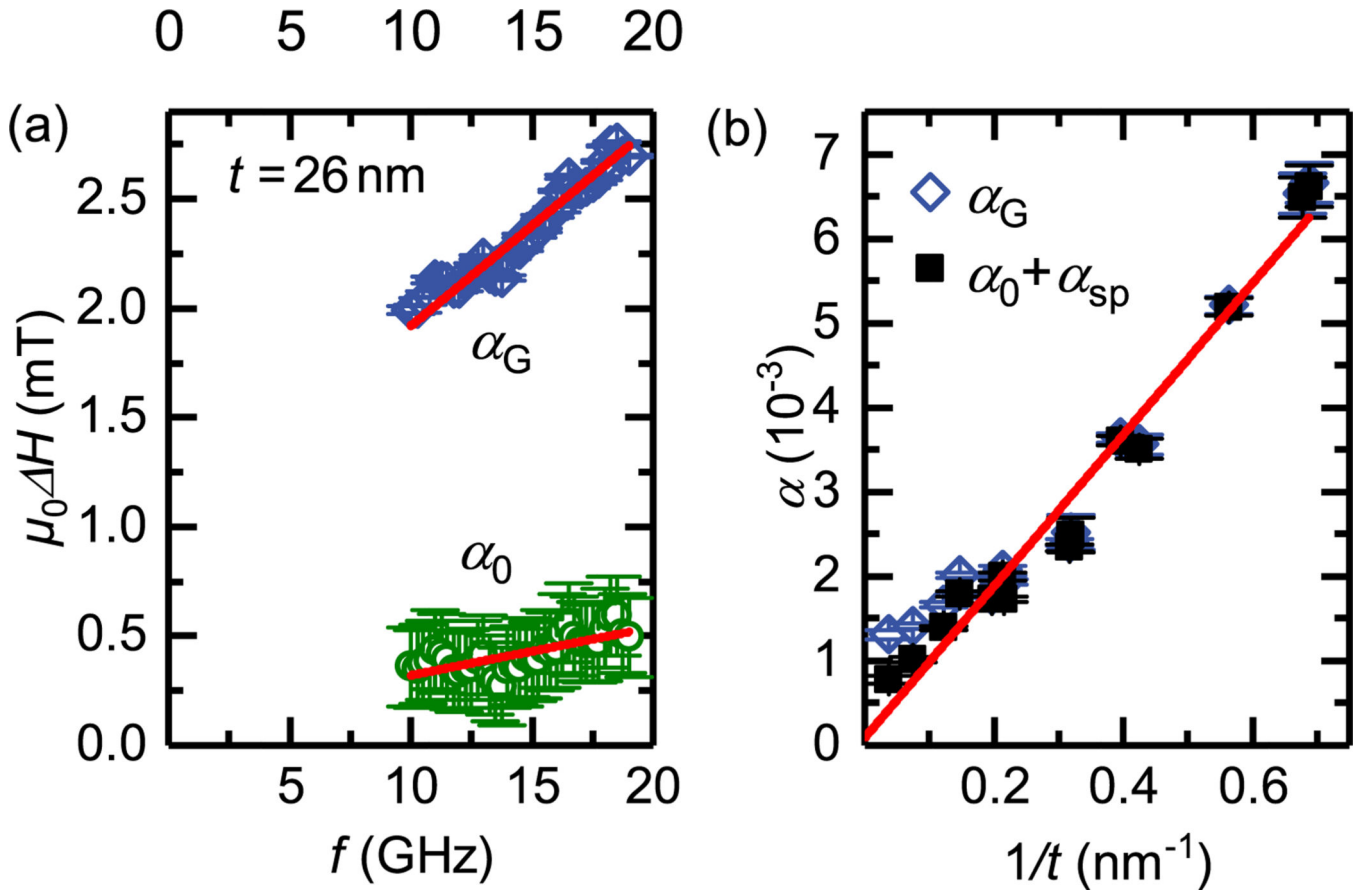

FIG. 2.

(a) An expanded view of the linewidth vs frequency plot of the $t = 26$ nm sample. The total linewidth is shown by the blue diamonds, from which the total Gilbert damping parameter α_G was extracted. The green circles represent the intrinsic linewidth contribution. In (b), the total damping α_G is plotted for different thicknesses t as blue diamonds. We subtracted the contributions from radiative damping and eddy currents and show the resulting $\alpha_0 + \alpha_{sp}$ as black squares. The red line is an unweighted fit to Eq. (7) in order to quantify the spin pumping contribution within our samples and to be able to extrapolate the intrinsic damping of CoFe within our multilayer system. For thicker samples, the available frequency range is rather small, leading to an increased uncertainty, as discussed in Ref. 32.

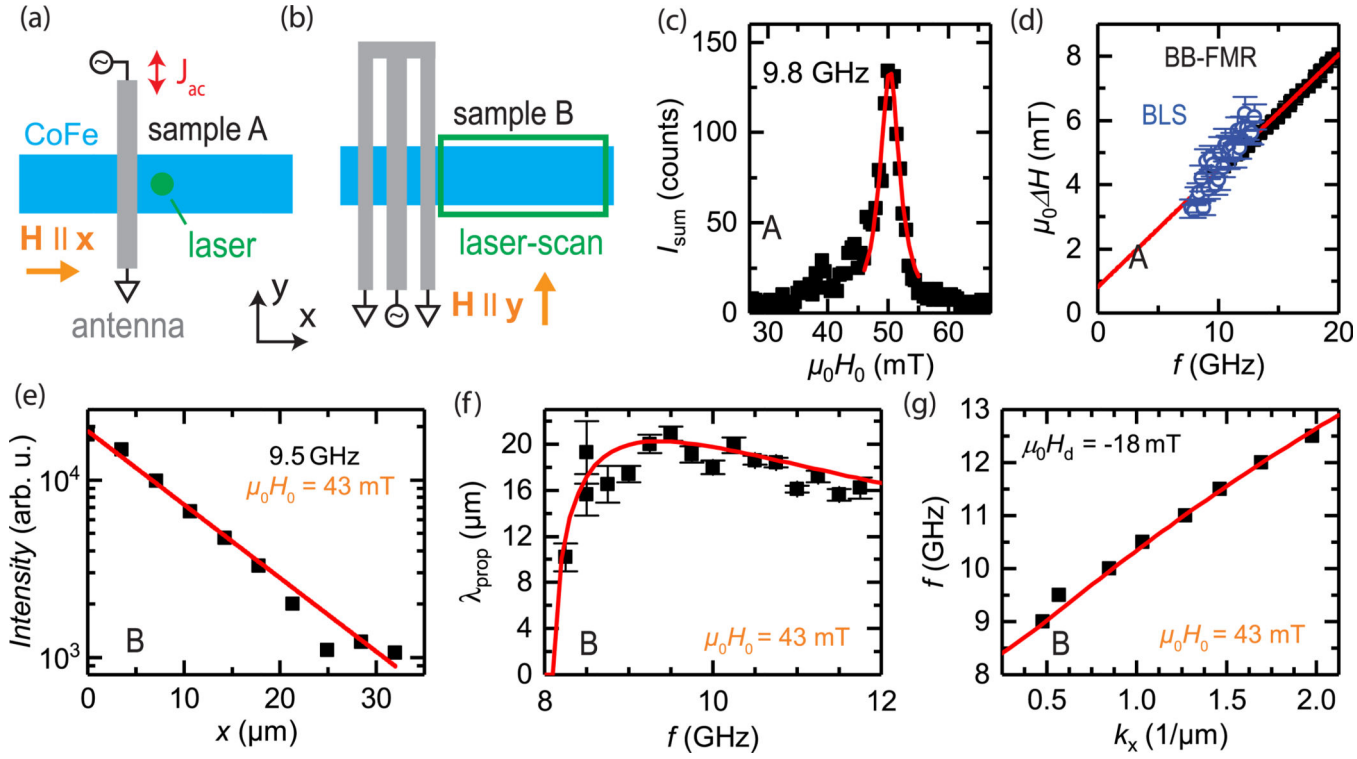

FIG. 3.

(a) and (b) Schematic top view of samples A and B, respectively. (c) Integrated BLS intensity vs field of sample A. By use of a Lorentzian fit (red line), the linewidth is extracted. In (d), we compare the BLS linewidth (open symbols) with the values obtained by in-plane BB-FMR on a blanket film (closed squares). (e) Representative dataset of sample B with f = 9.5 GHz. The BLS intensity was measured as a function of the position (x, y) in the area highlighted with the green rectangle in (b). The measured signal was then integrated in the y direction, and the exponential decay in the x direction is fitted (red curve). (f) Propagation length λ_{prop} for varying frequencies f. The depicted error bars are fit errors. The red curve is based on an analytical model calculation (see the text). (g) f vs k_x dispersion determined by phase-resolved μBLS. The red line is a model from Eq. (8).